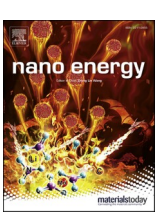
FISEVIER

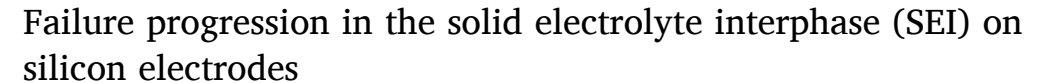
Contents lists available at ScienceDirect

Nano Energy

journal homepage: http://www.elsevier.com/locate/nanoen



Full paper



Kai Guo^{a,1}, Ravi Kumar^a, Xingcheng Xiao^b, Brian W. Sheldon^{a,*}, Huajian Gao^{a,2,3,**}

- a School of Engineering, Brown University, Providence, RI, 02912, USA
- b Chemical Sciences and Materials Systems Laboratory, General Motors Research and Development Center, Warren, MI, 48090, USA

ARTICLE INFO

Keywords: Lithium-ion batteries Electrodes Solid electrolyte interphase Fracture Interfacial delamination

ABSTRACT

Maintaining an electrochemically and mechanically stable solid electrolyte interphase (SEI) is of fundamental importance to the performance of high capacity anode materials such as silicon. In this study, a novel approach is utilized to apply controlled strains to SEI films on patterned Si electrodes. Mechanical failure mechanisms of SEI are investigated with integrated in situ AFM, ex situ FIB measurements and finite element modeling. Cross-sectional images reveal that the SEI has a bilayer structure, and through-thickness cracks appear inside of the outer SEI and arrest at the outer and inner SEI interface. The absence of cracking of the inner SEI layer implies that it has a high fracture toughness, and that it is possible to create an inner SEI which exhibits excellent strain tolerance compared to the outer layer. Interfacial delamination occurs between the outer and inner SEI layers while the inner layer is still well adhered to the underlying Si. The experimental and modeling results indicate that the inner SEI layer is sufficient for passivation of the Si surface. More broadly, the present work provides important guidelines for producing inner SEI layers that can simultaneously satisfy both electrochemical and mechanical criteria for long term passivation of silicon electrode surfaces.

1. Introduction

The passivation film formed on the surface of an electrode due to electrolyte decomposition, usually referred to as the solid electrolyte interphase (SEI), plays an essential role in the performance of Li-ion batteries. An ideal SEI layer should be electronically insulating, ionically conducting and mechanically stable. Graphite anodes expand by only $\sim \! 10\%$ when fully-lithiated. However, silicon (Si), one of the most prominent high energy density anode materials to replace graphite, undergoes colossal volume changes (up to 300%) during cyclic lithiation (lithium insertion) and delithiation (lithium extraction). This is believed to cause large deformation and mechanical degradation of SEI, and thus the SEI stability is widely recognized as a major roadblock for developing Si anodes. Substantial efforts have been devoted to improving SEI performance using electrolyte additives [1–3], encapsulation of Si particles [4–6], and artificial surface layers [7–9]. A large variety of

characterization techniques including X-ray photoelectron spectroscopy (XPS) [10–12], X-ray scattering [13], electrochemical impedance spectroscopy (EIS) [10,14–16], Raman spectroscopy [17], Secondary ion mass spectrometry (SIMS) [16,18], atomic force microscopy (AFM) [19–22], and cryo–electron microscopy [23–25] have also been employed to scrutinize the formation, evolution, and functionality of SEI layers. However, most existing studies focus on SEI chemistry and structure, while relatively few provide direct information about the mechanical integrity of the SEI.

Many prior studies report that the SEI that forms in carbonate electrolytes has a bilayer structure, with an outer layer that consists primarily of organic electrolyte decomposition products and an inner layer that contains more inorganic components (e.g., Li₂CO₃, LiF, etc) [16,20, 21,26–37]. Some work also suggests a mosaic-type SEI structure [38, 39]. The factors which cause these structures are not well understood, however, differences are likely to depend on the electrolyte composition

^{*} Corresponding author.

^{**} Corresponding author.

E-mail addresses: brian sheldon@brown.edu (B.W. Sheldon), huajian gao@brown.edu (H. Gao).

Laboratory for Atomistic and Molecular Mechanics (LAMM), Department of Civil and Environmental Engineering, Massachusetts Institute of Technology, Cambridge, MA 02139, USA.

² School of Mechanical and Aerospace Engineering, College of Engineering, Nanyang Technological University, 70 Nanyang Drive, Singapore 637457, Singapore.

 $^{^{3}\,}$ Institute of High Performance Computing, A*STAR, Singapore 138632, Singapore.

and cycling conditions. In this work we focus on the bilayer SEI structures that have been widely observed. These structures have not been carefully considered in the limited analysis of SEI failure mechanisms performed to date. For instance, He et al. performed a stress analysis of a heterogeneous elastic SEI [40], and Tanaka et al. studied the effect of plasticity on the mechanical failure of a homogenous SEI layer using the material point method [41]. Our work is based on careful experiments which demonstrate that the SEI exhibits behavior which can be viewed as a two layer system from a continuum mechanics perspective. This follows from our recent in situ AFM imaging which reveals extensive cracking of SEI layers in the "shear lag zone" (SLZ) that occurs near the edges of patterned Si islands [42]. Subsequent work shows that strain in the SEI layer leads to more lithium consumption [43]. While SEI failures on silicon particles are of great interest, controlled strains can not be directly applied to the SEI that forms inside of practical electrodes. In contrast, the patterned Si islands in our studies are an ideal platform to investigate the mechanical failure mechanisms of the SEI as they allow controlled strains to be applied to the surface layer, while at the same time preventing cracking in the underlying silicon by limiting its dimensions [44,45]. This platform provides a novel opportunity to conduct detailed studies of mechanical degradation of SEI and affords the type of mechanistic insight that is needed to make progress on understanding failure mechanisms that occur inside of particle-based electrodes. The work reported here is designed to shed further light on

The experimental observations reported here are based on AFM and FIB cross-sectional images of both SEI and cycled Si thin film electrodes. These provide the basis for a finite element model (FEM) of a bilayer SEI on a Si island, which can capture the observed failure behaviors. This continuum modeling elucidates the intrinsic mechanisms of the cracking, delamination and spallation of the outer SEI layer. This is a significant extension to previous work which models the mechanical failures of thin film and island electrodes [44,46–54]. These prior studies do not address cracking and delamination in SEI, phenomena which play a critical role in the capacity retention of silicon electrodes. The combined experimental and FEM results demonstrate that SEI films with a bilayer structure can be effectively described with a continuum mechanics framework. The model also provides a basis for more general considerations of failure processes in these structures, which are presented in the final section.

2. Methods

2.1. Experimental section

The patterned Si island samples for AFM investigations were prepared on $500\,\mu m$ thick quartz glass wafers (double-side polished, $40\,mm\times40\,mm$ in size). A bonding layer of $20\,nm$ thick Ti and a $200\,nm$ thick Cu current collector were deposited by electron beam evaporation, at a rate of $1\,\mbox{\normalfont\AAs}^{-1}$ for both metals. The Si patterned electrodes were fabricated by a standard lithographic process. The S1813 (Shipley Co.) photo resist was spin coated on the as-prepared Ti/Cu multilayer electrode and prebaked at $115\,^{\circ}\text{C}$ for $2\,\text{min}$. The exposure process was carried out by an ultraviolet mask aligner system (Karl Suss MA6, Germany). The samples were then developed in 1:1 mixture of MF312 and DI water for $1\,\text{min}$. Amorphous Si thin films were deposited by ebeam evaporation of pure Si pieces (P-type, 99.999%) at a rate of $1.5\,\mbox{\normalfont\AAs}^{-1}$. After deposition the remaining photoresist was removed by dipping the samples in acetone using slow agitation ultrasonication.

The in situ measurements were conducted with a Dimension ICON Electrochemical AFM setup inside an argon-filled glovebox (Nano Surfaces Division, Bruker), where both $\rm H_2O$ and $\rm O_2$ were below 1 ppm. The unique PeakForce tapping mode was used with MLCT tips (Bruker AFM Probes), composed of a silicon nitride cantilever with a sharp silicon nitride tip (spring constant: $\rm 0.6~N~m^{-1}$, nominal tip radius: $\rm 20~nm$). The electrolyte consisted of a mixture of ethylene carbonate (EC) and

dimethyl carbonate (DMC) (1:1 vol. ratio with 1 M LiPF6). The samples were cycled against Li metal foil in an in-house electrochemical AFM cell designed for lithium-ion battery materials that is sealed during AFM operation. These in situ cells contain significantly more electrolyte than a coin cell, and the current does not always provide an accurate measure of the state of charge [20]. For this reason, cycling was conducted with a sequence of potentiostatic holds. The cell was held at each potential until the current reached an asymptotic value that was less than 10% of the value at the start of the hold. SEI formation occurred primarily in the first cycle, during holds at 0.6, 0.3, 0.1, and 0.05 V that took a total time of approximately 4 h [42]. Previous work (with a different carbonate electrolyte) shows that variations in the duration of the first cycle produce significant differences in the SEI thickness and properties [20,21]. The SEI in the current study is relatively thick, but within the range of values reported in other work [55–57].

The cycled samples were also examined via post-mortem transmission electron microscopy (TEM, JEOL 2100F). A focused ion-beam (FIB, FEI HELIOS 600) was used to prepare these specimens using a lift-out technique, to create a cross-section of the cycled films.

2.2. Modeling Section

A finite element method (FEM) analysis was conducted using ABA-QUS (Dassault Systemes Simulia Corp., Providence, RI). A plane strain model (see Fig. S1a in the Supplementary material) was adopted to simulate a cross-section parallel to the side faces of the island, which consists of a bilayer SEI structure, a Si island electrode, a Cu current collector and a cohesive layer embedded between the Si and Cu. Taking advantage of the symmetry of the problem, only half of the island is considered. In situ AFM observations demonstrate that most of the SEI layer was formed prior to the Li-induced expansion of Si. Thus, the bilayer SEI is assumed to pre-exist with constant thickness and further SEI growth during cycling is neglected in the FEM model. Additionally, the SEI formed on the side of the island is not included.

The lithiated Si, Cu, and outer and inner SEI are assumed to be isotropic, elastic-perfectly plastic, and initially stress-free. The Young's modulus of the outer SEI is 2.3 GPa according to the AFM measurements (Fig. S2, Supplementary material), which is also consistent with previous reports [58]. We estimate that the Young's modulus of the inner SEI takes on a value in the range of 3–10 GPa, which is consistent with the reported range, including recent calculations via molecular dynamics (MD) simulations [59]. Very few previous studies have reported the stress-strain behaviors and yield stresses of SEI. Recently, Yoon et al. found that an SEI-like film formed from lithium-electrolyte reactions exhibits elastic-perfectly plastic behavior with a yielding stress of approximately 10 MPa [60]. In this work, we assume that the yield stresses of the outer and inner SEI are both near 1% of their Young's moduli. Thus, the outer SEI yields at 23 MPa, and the stiffer inner SEI yields at a higher stress.

The cohesive layers adopted in our FEM models follow a triangular softening law (Fig. S1b, Supplementary material), which is defined by an initial elastic stiffness K, the peak traction t^0 , and the area of the triangle representing fracture toughness Γ . In the modeling, the initial elastic stiffness is constant and much larger than the stiffnesses of the adjacent materials to avoid artificial compliance from introduction of the cohesive layer. The separation at complete failure δ^f is equal to four times the separation at the initiation of degradation δ^0 . The cohesive properties are assumed to be identical under tension and shear, and we ignore the effect of mode mixity. A cohesive layer is embedded to simulate interfacial delamination between the Si and Cu. In this case, the peak traction and fracture toughness of the cohesive law are calibrated based on the experimental observation that the length of the delaminated Si is approximately 1 µm after 5 cycles. The properties of cohesive layers embedded in the SEI layer are not available in the literature due to the difficulties of measuring SEI toughness. Therefore, we tune the fracture

toughness Γ in a reasonable range and assume that the triangular shape for the cohesive law is always self-similar. That is, for a given fracture toughness, the peak traction can be calculated by using this relationship: $t^0 = \sqrt{\Gamma K/2}$.

Table 1 lists the geometrical parameters and material properties used in the model. The bottom surface of the Cu is fixed. The 4-node bilinear plane strain quadrilateral hybrid elements (CPE4H) and 4-node twodimensional cohesive elements (COH2D4) are assigned to the bulk materials and cohesive layers, respectively. For the relatively thin Si and the low cycling rates used in the experiments, prior work indicates that the Si fully lithiates with a relatively uniform concentration profile (i.e., Li diffusion is fast) [42,43]. Thus, the state of charge (SOC) is assumed to be uniform in the Si. It is difficult to precisely determine the Li content of the Si during the AFM experiments. At 0.05 V, the SOC is believed to be between 0.6 and 0.9 (the lower estimate is based on the measured height increase in the middle of the island and the upper bound is roughly equal to the equilibrium SOC at this potential). For the simulations reported here, using the lower bound SOC along with a standard literature value for the partial molar volume of Li [22] gives results which match the volume expansion observed in the experiments. If the SOC at 0.05 V is higher, then the observed volume expansion implies that the Li partial molar volume must be lower to match the experiments. Running simulations with these alternative parameters gives nearly identical results.

3. Experimental results

We previously reported in situ and operando AFM imaging of patterned Si islands where extensive SEI cracking occurred in the SLZ near the island edges [42]. The experiments reported here build on this earlier study and investigate the SEI layer under repeated expansion and contraction of the underlying Si. The cycled samples were also analyzed using ex situ FIB cross-sections to understand key characteristics of the SEI failure modes. These observations provide the basis for detailed models of SEI failure modes that are presented in section 4.

To obtain a more accurate understanding of SEI delamination due to repeated expansion and contraction of the underlying Si, the patterned islands were subjected to multiple cycles. During the first three cycles, SEI cracking in the SLZ was observed in AFM images (see more details in the Supplementary material). Fig. 1 shows 2D AFM surface topographs of patterned Si islands during the 4th and 5th cycles. The first point to note in Fig. 1(a) (start of 0.05 V hold) is that parts of the SEI layer from the corners of the island have already delaminated from the surface due to repeated expansion and contraction of the underlying Si.

With more Li-insertion the underlying Si expands further laterally, and Fig. 1(b-e) shows that other regions of the SEI in the SLZ also

Table 1Geometrical parameters and material properties adopted in the FEM model.

Island half length	7.5 μm	This work
Si thickness (before cycling)	225 nm	This work
Outer SEI thickness	460 nm	This work
Inner SEI thickness	110 nm	This work
Cu thickness	200 nm	This work
Maximum SOC in Li _x Si	0.6	This work
Li _x Si Young's modulus	$90 \text{ GPa (SOC} = 0) \sim 42 \text{ GPa}$	[69]
	(SOC = 0.6)	
Li _x Si Poisson's ratio	0.26	[69]
Li _x Si yield stress	1.75 GPa	[70]
Outer SEI Young's modulus	2.3 GPa	This work
Inner SEI Young's modulus	3-10 GPa	Estimated
SEI elastic strain at yield point	1%	Estimated
SEI Poisson's ratio	0.3	Estimated
Cu Young's modulus	128 GPa	[71]
Cu Poisson's ratio	0.36	[71]
Cu yield stress	876 MPa	[72]
Si/Cu interfacial peak traction	1 GPa	Calibrated
Si/Cu interfacial fracture	$40 \mathrm{J} \mathrm{m}^{-2}$	Calibrated
toughness		

undergo delamination. The spallation observed here occurred in less than $\sim\!20\%$ of the islands during the fourth cycle. To further clarify this behavior, the scan size was reduced to $5~\mu m \times 5~\mu m$ to obtain higher resolution images of SEI cracking and delamination from the top right corner of the island. Fig. 2(a–c) shows consecutive scans before, during and after the SEI delamination occurring in the 0.05 V hold. Fig. 2(d) shows the DMT modulus map that corresponds to Fig. 2(a) (beginning of 0.05 V hold). This is obtained from the measured force-displacement relationships [58], and here this indicates that part of the SEI layer in the top right corner is very soft compared to the other regions. The low stiffness in the dark region appears to be caused by loose attachment of the SEI layer, which is consistent with the subsequent scans which show that this soft region delaminates from the surface. This suggests that the repeated expansion and contraction of the Si causes interfacial (Li_xSi/SEI) instabilities which result in loosely attached SEI.

Fig. 2(e) shows the evolution of the height profiles in the region where SEI delamination occurs (marked by white dotted lines in Fig. 2 (a–c)). After this piece of the layer is removed the thickness difference between the surfaces is ~500 nm. The key observation here is that after the SEI delaminates, there is no measured height change in the region where the spallation occurred. This indicates that there is no detectable regrowth of the SEI after the delaminated layer is removed, which implies that the electrode surface is still passivated. A logical interpretation here is that spallation only removes the outer portion of the SEI, and that an inner layer protecting the Si is still intact on this area of the electrode surface. This indicates that delamination occurs at the interface between the outer and inner layers. It also indicates that the remaining inner SEI layer passivates the Si surface (i.e., because the SEI thickness does not increase here during subsequent cycling).

The bilayer SEI structure used to explain these observations has been widely discussed in previous work. Some researchers have suggested that the outer and inner layers are comprised of organic and inorganic decomposition products, respectively [16,26-37]. We previously proposed that both the outer and inner layers are nanocomposites that can contain both organic (e.g., Li ethylene dicarbonate, etc) and inorganic phases (e.g, Li₂CO₃, LiF, etc), where the inorganic constituents that are necessary for passivation are more prevalent in the inner region [20,21, 42,43]. This stems from the knowledge that initial electrolyte decomposition produces organic material at higher potentials [16], such that the formation of inorganic constituents at lower potentials inside of this matrix is then likely to produce a nanocomposite inner layer [20]. This is consistent with the observations in Fig. 2, where the inner region in the SLZ withstands large strains (>10%) while still providing good passivation. In contrast a dense inner layer consisting of only the ceramic (i.e., inorganic) phases should not survive the large strains that are applied to the SEI by volume changes in the underlying silicon electrode.

To verify our interpretation of the AFM surface topographs and height profiles, cycled islands after 5 full cycles (different from the island shown in Fig. 1) were also examined ex situ with FIB cross-sections. Fig. 3 shows images from cuts that were made diagonally across the cycled islands. The quartz glass wafer, Cu current collector layer, Si, inner and outer SEI were all identified with energy-dispersive X-ray spectroscopy (EDS) line scans (below the Pt top layer that was deposited to provide protection from the Ga⁺ ions). It is important to note that during lihiation, through-thickness cracking in the underlying Si should not occur because it is in compression; in contrast to the tensile stresses in the SEI. Tensile stresses that develop in the Si during delithiation can result in through thickness cracks, however, this was not observed. The FIB cross-sections in Fig. 3 reveal that the through thickness cracks here are limited to the SEI. The images also show that the SEI layer in the center of island is well adhered to the Si surface, without any evidence of cracking. The cracks through the SEI in the SLZ are also consistent with the top view AFM images in our previous report [42].

Cracking of the SEI layer occurs during lithiation where the SEI is in tension (see Figs. S3b and d in the Supplementary material). These cracks remain open with further lithiation and are not healed by

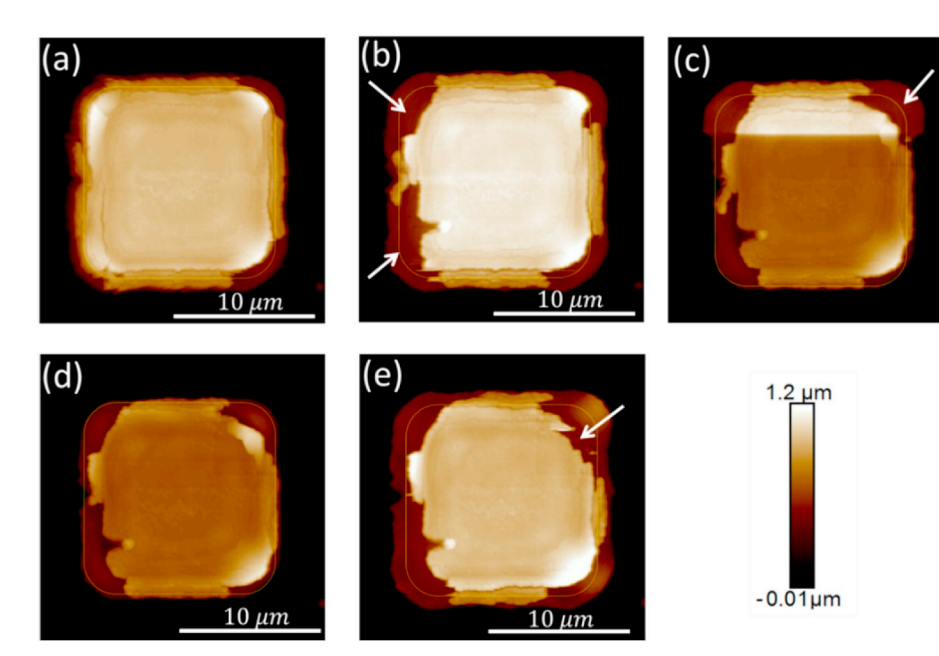


Fig. 1. 2D AFM surface topographs of patterned a-Si electrode (a) during the 4th lithiation cycle at the beginning of the 0.05 V hold; (b) scan at 0.05 V after 5 h and 26 min; (c) upper part shows end of 0.05 V hold (fully lithiated) and lower part shows initial scan at 1.5 V (during delithiation); (d) scan at the end of 1.5 V hold, (e) during 5th lithiation cycle at the end of the 0.05 V hold. The arrows indicate areas where the SEI undergoes delamination. These images show that there is a clear height difference after delamination of the SEI. The dotted yellow box indicates the original size of the island and is useful in visualizing the lateral expansion and contraction of the islands during cycling.

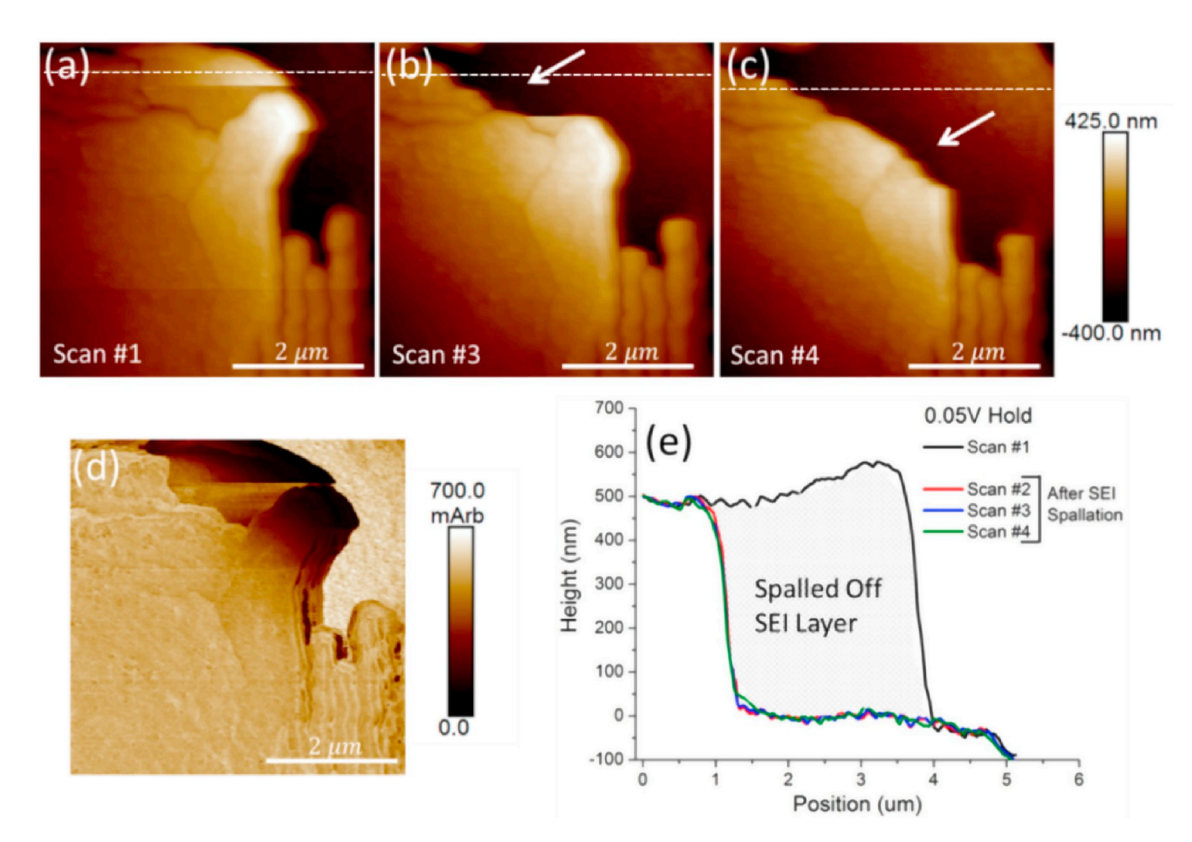


Fig. 2. 2D AFM surface topographs of top right corner of the patterned island in Fig. 1, during the 4th lithiation cycle at 0.05 V: (a) scan #1, (b) scan #3, and (c) scan #4. After scan #1, part of the SEI from the corner region delaminates, as indicated by white arrows in (b) and (c). Image (d) is the DMT modulus map for image (a), which clearly shows that the part of the SEI layer which delaminates is loosely attached (i.e. it is much softer compared to other areas). Image (e) shows the height evolution of the line section (white dotted line in (a)–(c)). There is no new SEI growth on the exposed surface after spallation.

additional SEI formation suggesting that either the cracks do not reach the Si/SEI interface or that the newly formed SEI here is thin and passivating. With further cycling these cracks penetrate further into the SEI layer and result in partial delamination of the outer layer. Therefore, delamination can be driven by both lithiation and delithiation induced stresses in the SEI layer. A careful examination of Fig. 3 shows that a thin SEI layer is still present on top of the underlying Si surface, after the

outer layer has delaminated. There is limited image contrast between the different layers, but an inner and outer layer are seen above the silicon in Fig. 3(a). The delamination crack on the right side of this image runs between these inner and outer layers. These observations support the assertion that SEI delamination occurs along the interface between the outer and inner SEI layers rather than between the inner SEI and underlying Si. Another important observation is that this inner layer

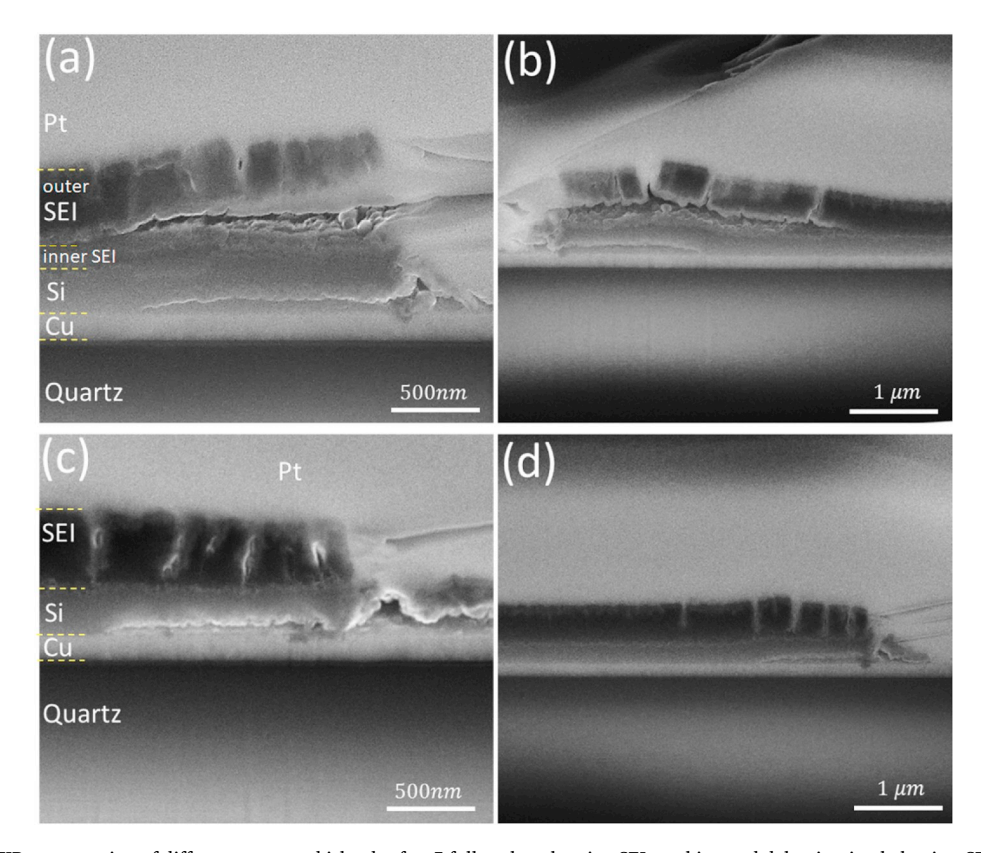


Fig. 3. (a–d) Diagonal FIB cross-section of different patterned islands after 5 full cycles, showing SEI cracking and delamination behavior. SEI is also observed on the sides of the islands (these surfaces are also passivated). The cross-sections also show partial delamination of Si from the Cu current collector in the SLZ. It is not known if this occurs during post-cycling sample preparation (i.e., FIB cutting).

is thinner than the outer layer. The inner layer that remains on top of the Si after delamination of the outer layer is also consistent with Fig. 2(e), which shows that SEI does not regrow after spallation (i.e., if the Si surface were re-exposed to the electrolyte at 0.05 V, then SEI regrowth would cause an increase in thickness). Based on these observations, the thin inner layer is sufficient for passivation of Si surfaces and exhibits much more strain tolerance compared to the outer layer.

The bilayer SEI structure described above is consistent with all of the experimental observations. As outlined above, the images in Fig. 3 indicate that the inner layer adheres to the underlying Si surface, while the outer layer delaminates during repeated cycling. Ex situ transmission electron micrsocopy (TEM) was performed to confirm this film structure. The cross-sectional image of the center region from a cycled island in Fig. 4(a) shows clear contrast difference between the inner and outer layers (note that the layer thicknesses here are similar to those seen in Fig. 3(a)). The first point to note from the TEM images is that the SEI thickness is similar in the center and in the SLZ. This is consistent with the interpretation that the strain in the SLZ enhances the formation of SEI constituents inside of the mesoporous structure as hypothesized in our previous work [43]. As noted, above the interface between the outer and inner SEI is also consistent with the explanation of Fig. 2. Selected area electron diffraction patterns (Fig. 4(c)) show that fine-grained LiF is present in both the inner and outer SEI layers (based on the diffraction ring spacings). EDS did not provide a meaningful comparison between the composition of the inner and outer layers. This is not suprising, since the SEI is primarily composed of light elements which are difficult to detect with this technique.

The combined experimental observations reported here demonstrate that SEI failure modes are potentially complex. As already noted, there are a number of other reports which support the idea of bilayer structures. The results in Fig. 2(e) provide strong evidence for the stability of an inner passivation layer, where SEI growth does not occur after

spallation of the outer layer. The sequence of events leading to this are clarified with the other observations in Figs. 1–4. With these types of bilayer structures, there are also other fracture and delamination processes that may occur under other conditions. This range of possibilities provides a strong motivation for developing a mechanics-based framework to evaluate SEI failure mechanisms in more detail. The modeling in the next section is first designed to provide an accurate assessment of the observations in our experiments. This is then employed to provide a broader assessment of SEI failure mechanisms in section 4.5.

4. Analysis

4.1. Stress and strain distribution in the SEI layer

To interpret the observed through-thickness cracking of the outer SEI layer, FEM simulations were performed to estimate the distribution of in-plane stress and strain in the SEI layer, as shown in Fig. 5 (more details of the FEM model are discussed in the Modeling Section). No inplane deformation occurs in the island center, but in the SLZ, the Si island can undergo lateral expansion during lithiation, which stretches the SEI layer. At the beginning of lithiation (i.e., the state of charge, SOC = 0.1), the outer SEI is subjected to elastic deformation, Fig. 5(a) shows that the maximum in-plane stress in the outer SEI is located at its top surface with a distance of approximately 1 µm from the island edge, which agrees with where the surface cracking was observed in the AFM images (Fig. S3). The in-plane stress and strain profiles along the top surface of the outer SEI are plotted in Fig. 5(b) and (c), respectively. As lithiation proceeds, extensive plastic deformation occurs in the transition region between the island center and the SLZ, where the in-plane stress is limited by the yield stress of the outer SEI (Fig. 5(b)). After the 1st lithiation cycle (SOC = 0.6), the in-plane strain reaches a maximum value of $\sim 13\%$ (Fig. 5(c)) at the same position where the

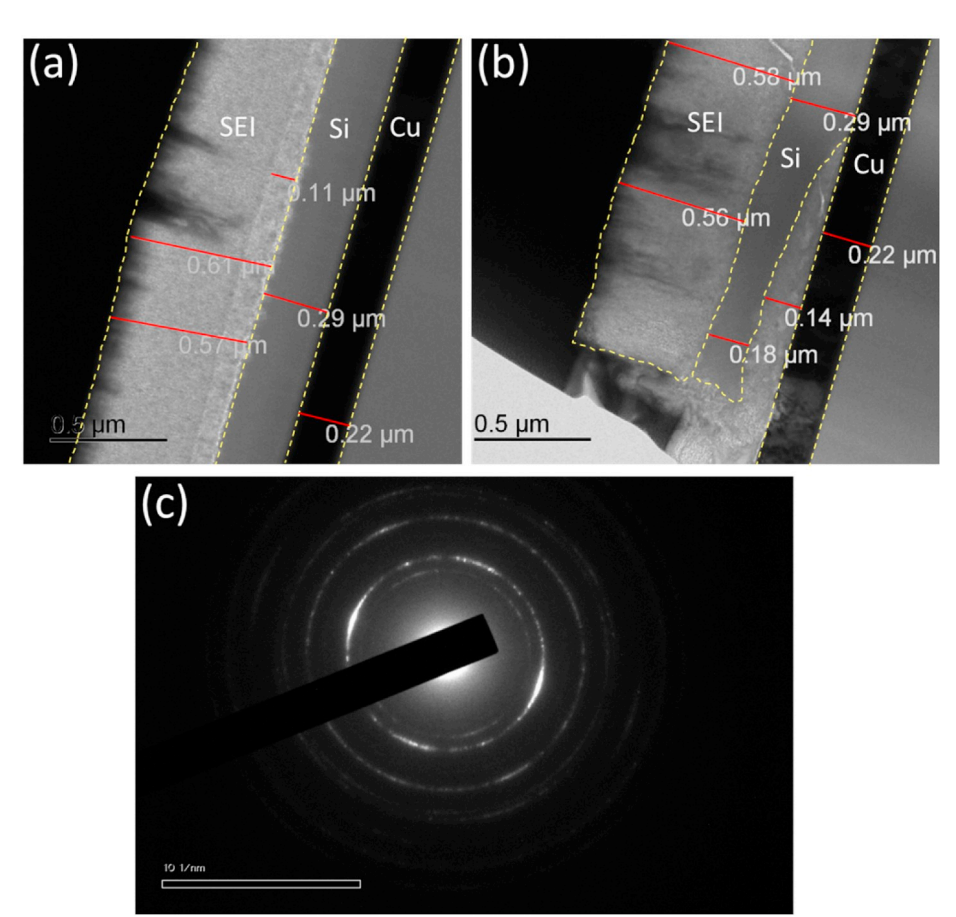


Fig. 4. TEM images showing the cross-section of a cycled patterned island (a) at center and (b) in the shear lag zone (corner). Near this edge, SEI is also observed between the Si and Cu (the soft nature of this SEI layer may lower the sliding resistance in the SLZ); (c) electron diffraction pattern from the inner SEI layer.

maximum in-plane stress is located at SOC = 0.1. The simulation results suggest that cracking is likely initiated at the SEI surface with a certain distance from the island edge. The intrinsic surface cracking mechanisms in the SEI are still an open question that require a separate study.

4.2. Fracture resistance of the inner SEI layer

Close examination of the FIB cross-sections in Fig. 3 shows that through-thickness cracks do not reach the Si surface. Within the resolution limits of these images, it appears that crack arrest occurs at or close to the interface between the outer and inner SEI layers. The FEM results in Fig. 5(a) also show that the stiffer inner SEI experiences higher in-plane stress than the outer SEI. To interpret the experimental observations, the FEM is slightly modified as schematically shown in Fig. 6(a). A through-thickness crack that penetrates the outer SEI is located where the maximum surface tensile stress is predicted in Fig. 5(a), and a through-thickness cohesive layer is embedded in the inner SEI right underneath the crack tip to simulate potential cracking of the inner SEI layer.

To investigate whether a through-thickness crack penetrates into the inner SEI within 5 cycles, a series of FEM simulations were performed with different values for Young's modulus and fracture toughness of the inner SEI. This analysis focuses on the point where fracture events first occur, and does address post-fracture changes in the underlying electrode. For example enhanced Li ion conduction in the vicinity of the crack is likely to perturb the electrode/SEI interface near the crack. These more complex coupling effects between Li conduction and SEI fractures are not considered here and will be left for future study.

Selected properties are correlated in this analysis. The yield stress of the inner SEI is taken to be proportional to its modulus. We also assume that the adopted triangular cohesive law is self-similar when tuning the fracture toughness of the inner SEI, i.e., the peak traction is proportional to the square root of the fracture toughness. The findings are summarized in a failure map in Fig. 6(b), which shows a linear boundary between the "penetration" and "no penetration" regimes. The observation that through-thickness cracks are arrested at the outer and inner SEI interface suggests that the inner SEI has a sufficiently high fracture toughness which lies in the "no penetration" regime.

4.3. Delamination of the SEI layer

Another observation from the FIB cross-sections (Fig. 3) is that the outer and inner SEI interface (IntOI) delaminates while the interface between the inner SEI and Si (IntIS) remains well bonded. The FEM was modified to account for delamination of the outer or inner SEI layers, as schematically shown in Fig. 7(a). Two horizontal cohesive layers are embedded along IntOI and IntIS. Similar to the model discussed in the previous section, a through-thickness crack is arrested at IntOI, but the inner SEI is considered to be sufficiently tough and thus no through-thickness cohesive layer is included.

The fracture toughness values of IntOI and IntIS were tuned to evaluate whether interfacial delamination occurs in 5 cycles. The triangular cohesive law for each interface is still self-similar, but with varying fracture toughness. Fig. 7(b) shows a delamination map with the Young's modulus of the inner SEI fixed at 5 GPa. Towards the top right corner the interfacial toughness is high and neither of the two interfaces of interest are delaminated. When one interface is weak and the other is tough, delamination occurs at the weak interface. If IntIS is the weaker interface, its delamination initiates from the island edge due to extensive shearing between the SEI and expanding Si. Towards the bottom left

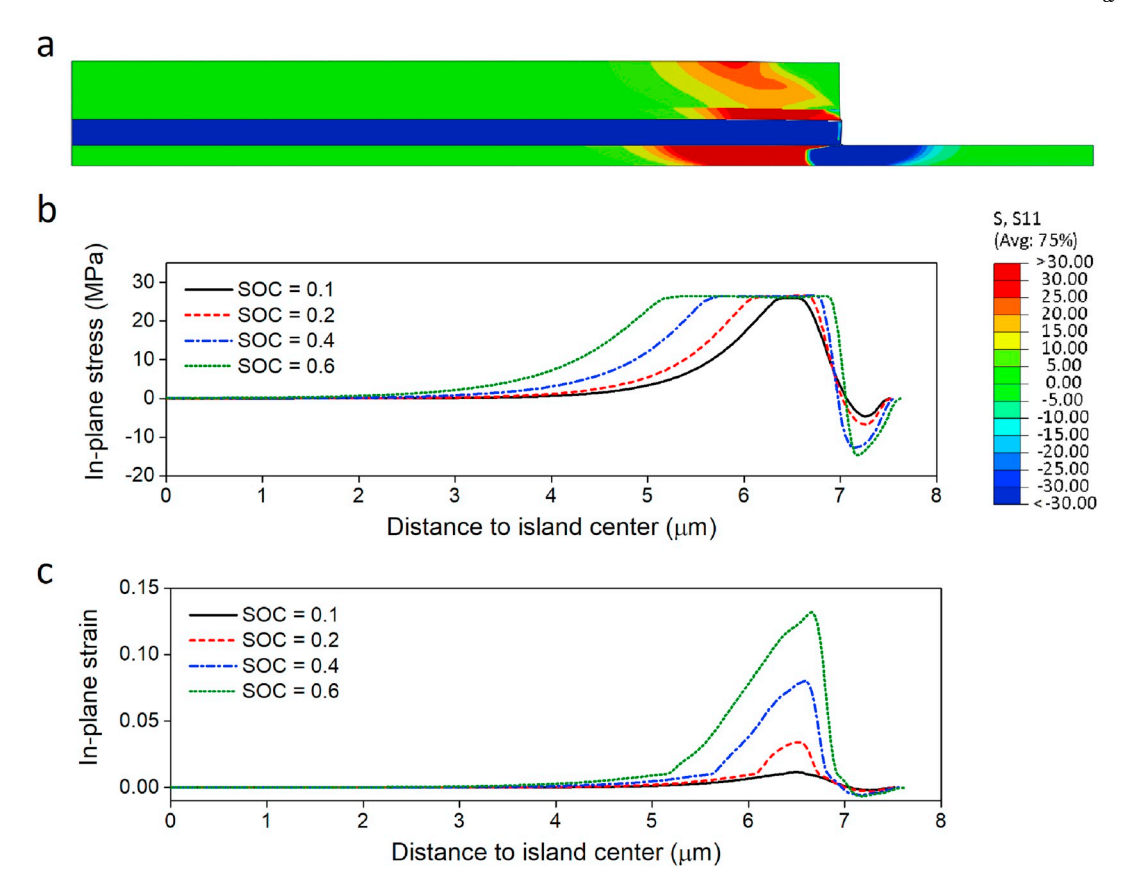


Fig. 5. (a) Contour plot of in-plane stress (MPa) during the 1st lithiation cycle at SOC = 0.1; (b) In-plane stress and (c) in-plane strain profiles along the top surface of the SEI layer during the 1st lithiation cycle. The Young's modulus of the inner SEI is 5 GPa.

corner of the map, when both interfaces are weak, a boundary (red dashed line) occurs that divides the outer/inner SEI and SEI/Si delamination regimes. If one interface delaminates first, the other interface remains bonded because the energy stored in the inner SEI has been released. However, it is still possible that delamination of both interfaces occurs, as shown in the bottom left corner of the map. Based on the results of the FIB cross-sections and this delamination map, it appears that the toughness of IntIS is much higher than that of IntOI.

Another interesting finding is that the outer/inner SEI delamination regime has two sub-regimes divided by a vertical boundary (orange dotted line), which represents a critical IntOI toughness. If this toughness exceeds the critical value, the delamination between the outer and inner SEI initiates from the island edge, but if it is less than the critical toughness, the through-thickness crack deflects to propagate along IntOI, resulting in delamination. Due to the complex stress state in the island, it is difficult to address questions about why this bifurcation occurs and which parameters control the critical toughness. However, FIB cross-sections of different samples (see Figs. 3 and S4 in the Supplementary material) show that both of these two delamination modes can occur.

A delamination map with the Young's modulus of the inner SEI taken as 10 GPa is shown in Fig. S5 in the Supplementary material. Comparison of Figs. 7b and S5 reveals that reducing the modulus of the inner SEI layer increases the "no delamination" regime due to the lower strain energy released by interfacial delamination.

4.4. Spallation of the outer SEI layer

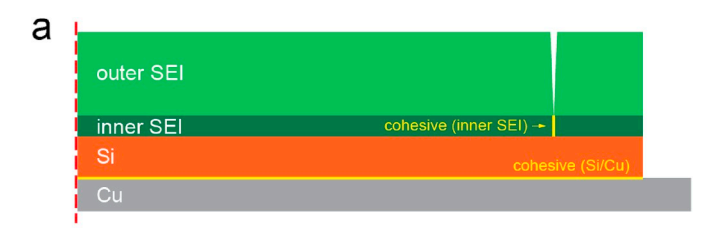
In certain FIB cross-sections (e.g., Fig. 3(b)), it is difficult to determine whether delamination of the outer SEI initiates from a throughthickness crack or from the island edge. However, the image in Fig. S4 clearly shows that in this sample the outer and inner SEI delamination

initiates from the tip of a through-thickness crack. To account for this behavior, we use a model with a cohesive layer embedded at IntOI while IntIS and the inner SEI itself are considered to be tough. The Young's modulus of the inner SEI is taken as 5 GPa and the toughness of IntOI is $0.012\,\mathrm{J\,m^{-2}}$. Fig. 8 shows sequential screenshots from the FEM simulation that depict the evolution of the interfacial delamination and spallation of the outer SEI.

During the 1st lithiation cycle (Fig. 8(b)), the SLZ of the Si island expands in both the lateral and thickness directions, while the center of the island can expand only along the thickness direction. Thus, the center of the island becomes thicker than the SLZ, and in the transition region between them, the IntOI is curved, which induces tensile stress normal to the interface and in turn results in delamination towards the center of the island (red arrow in Fig. 8(b)).

The crack closes but does not heal after the 1st delithiation cycle (Fig. 8(c)). Additionally, the edge of the Si buckles and delaminates from the underlying Cu substrate. The delaminated Si, no longer constrained by the Cu, shrinks more profoundly during delithiation than its lateral expansion during lithiation. Therefore, the two pieces of the outer SEI, divided by the through-thickness crack, are in contact during the end of delithiation. In this period, the outer SEI near the center pushes the outer SEI in the SLZ, inducing interfacial shearing between the outer and inner SEI layers. The friction coefficient between free surfaces of the fractured SEI is assumed to be 0.1.

During the 2nd cycle, the interfacial delamination initiated from the crack tip towards the island edge follows a two-step process (indicated by two orange arrows in Fig. 8(d,e)). Fig. 8(d) shows that during lithiation, the curvature of IntOI induces tensile stress in the SLZ, leading to delamination. During the 2nd delithiation cycle, the outer SEI in the SLZ is pushed by the outer SEI near the center again (Fig. 8(e)), shearing the remaining bonded area between the outer and inner SEI near the edge, and eventually leading to spallation of the outer SEI (Fig. 8(f)).



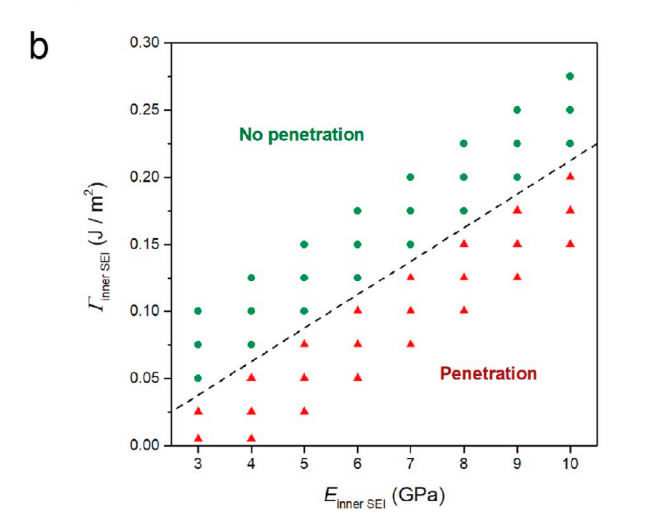


Fig. 6. (a) Schematic adopted for the FEM. (b) Failure map of crack penetration in the inner SEI (x- and y-axes correspond to the Young's modulus and fracture toughness of the inner SEI, respectively). Green dots denote no degradation in the cohesive layer embedded in the inner SEI, and red dots indicate that the cohesive layer is fully degraded (i.e., the through-thickness crack penetrates into the inner SEI).

The simulation results provide a possible explanation for the accumulative spallation that was observed in Fig. 1. After the 1st cycle, the delaminated Si is nearly free-standing, and the portion of the Si adjacent to it becomes new SLZ. Thus, additional Si delaminates from the Cu during the 2nd delithiation cycle, and the size of the delaminated Si in Fig. 8(e) is larger than that in Fig. 8(c). This delamination of Si is stable (i.e., not a drastic failure) due to the energy dissipation of plastic shearing of the top layer of the Cu. The incremental delamination between the Si and Cu causes the SLZ to move toward the center of the island, and as a result, the outer SEI incrementally delaminates from the inner SEI each cycle. Such accumulative failure can be related to the so-called ratcheting phenomenon which occurs in a variety of systems under cyclic thermal/mechanical loadings.

4.5. Failure progression in bilayer SEI

The experiments and analyses in the previous sections highlight key aspects of the failure processes that affect bilayer SEI structures. The validity of this continuum mechanics modeling is established by its ability to describe the phenomena observed in the specific experiments reported in section 3. The complex behaviors that occur here also imply that a range of failure sequences are possible in bilayer SEI films. These are summarized schematically in Fig. 9(a-g). A surface crack that penetrates the outer layer (mode a) can stop at the interface between the outer and inner layers if the fracture resistances for this interface and for the inner layer are both sufficiently high. If the crack is not fully arrested at this interface, one possibility is that the crack continues to run through the inner layer if its fracture resistance is low (mode b) and can then lead to delamination of the bilayer SEI from the electrode (*mode c*). Another possibility is that the surface crack deviates and causes delamination (mode d) and spallation (mode e) of the outer layer if the interface between the outer and inner layers is weak. After this

spallation, surface cracking ($mode\ f$) and delamination ($mode\ g$) of the remaining inner layer may still occur upon further lithiation of the electrode.

Among the failure processes shown in Fig. 9, those leading to delamination at the electrode surface ($modes\ c$ and g) are the most crucial phenomena to avoid. Both of these permit additional SEI formation on freshly exposed electrode surfaces, which leads to capacity fading. Similarly, $modes\ b$ and f are also potentially problematic, however, this fracture of the inner SEI can be tolerated if crack arrest occurs at the electrode interface.

To determine how these modes complete with each other (*mode b* vs. mode d, etc), failure criteria for the different modes were evaluated. We consider a bilayer SEI on a semi-infinite electrode which closely resembles the experimental configuration. The bilayer SEI and electrode undergo only elastic deformation, which is overly simplistic compared to the FEM simulations where plasticity is considered. However, this makes it possible to capture a broader general picture of failure criteria based on existing results from linear elastic fracture mechanics (LEFM). where through-thickness and interfacial cracking problems in thin film/ substrate systems have been well studied in the past three decades [61–68]. To further simplify this treatment, the outer and inner SEI layers are assumed to have the same Young's modulus E_f and Poisson's ratio ν_f . The key difference between the layers is then the fracture toughness values. The interface between the layers then plays an important role, particularly in the analysis of crack channeling presented below. The semi-analytical solution of energy release rate of a plane strain through-thickness crack in a single-layer thin film on a semi-infinite substrate is given by [65]:

$$g = \frac{\sigma_f^2 h_f}{\overline{E}_f} \tilde{g}\left(\frac{E_f}{E_s}, \nu_f, \nu_s, \tilde{a}_f\right),\tag{1}$$

where h_f is the total SEI thickness, $\overline{E}_f = E_f/(1-\nu_f^2)$ the plane strain modulus of the SEI, \tilde{a}_f the crack length normalized by h_f , and E_s and ν_s are the Young's modulus and Poisson's ratio of the electrode, respectively. The mismatch stress in the SEI, σ_f , is primarily caused by volume changes in the electrode during cycling, along with additional contributions from the formation of SEI constituents inside of the layers. The basic treatment presented here uses the results in Ye et al. [65] with $E_f/E_s=1/9,\ \nu_f=\nu_s=1/3$. Other modulus ratios can also be evaluated, but this case is sufficient for the treatment presented here. Here the normalized energy release rate \tilde{g} is only a function of \tilde{a}_f , which is given by:

$$\tilde{g}(\tilde{a}_f) = 3.951\tilde{a}_f(1 - \tilde{a}_f)^{0.3}(1 - 0.0784\tilde{a}_f)^2.$$
 (2)

Once the energy release rate of a plane strain crack given by Equation (1) exceeds the fracture toughness of the outer layer, isolated and stabilized surface cracks occur [62]. However, the through-thickness cracking in *modes a*, *b* and *f* are likely to occur by crack channeling, which is unstable and thus more detrimental. This occurs once the SEI fracture toughness is less than the energy release rate of a steady-state channeling crack, which can be calculated by integrating the energy release rate of a plane strain crack as follows [62],

$$G = \frac{1}{h} \int_0^h g(a) \, \mathrm{d}a. \tag{3}$$

For $mode\ a$, the energy release rate of a steady-state channeling crack in an outer layer of thickness h_0 is expressed as,

$$G^{a} = \frac{\sigma_{f}^{2} h_{f}}{\overline{E}_{f}} \frac{\int_{0}^{\xi_{o}} \tilde{g}(\tilde{a}_{f}) \, d\tilde{a}_{f}}{\xi_{o}}, \tag{4}$$

where $\xi_0 = h_0/h_f$ is the thickness fraction of the outer layer.

For $mode\ b$, a channeling crack propagates in the inner layer under an existing channel in the outer layer. Here the energy release rate at

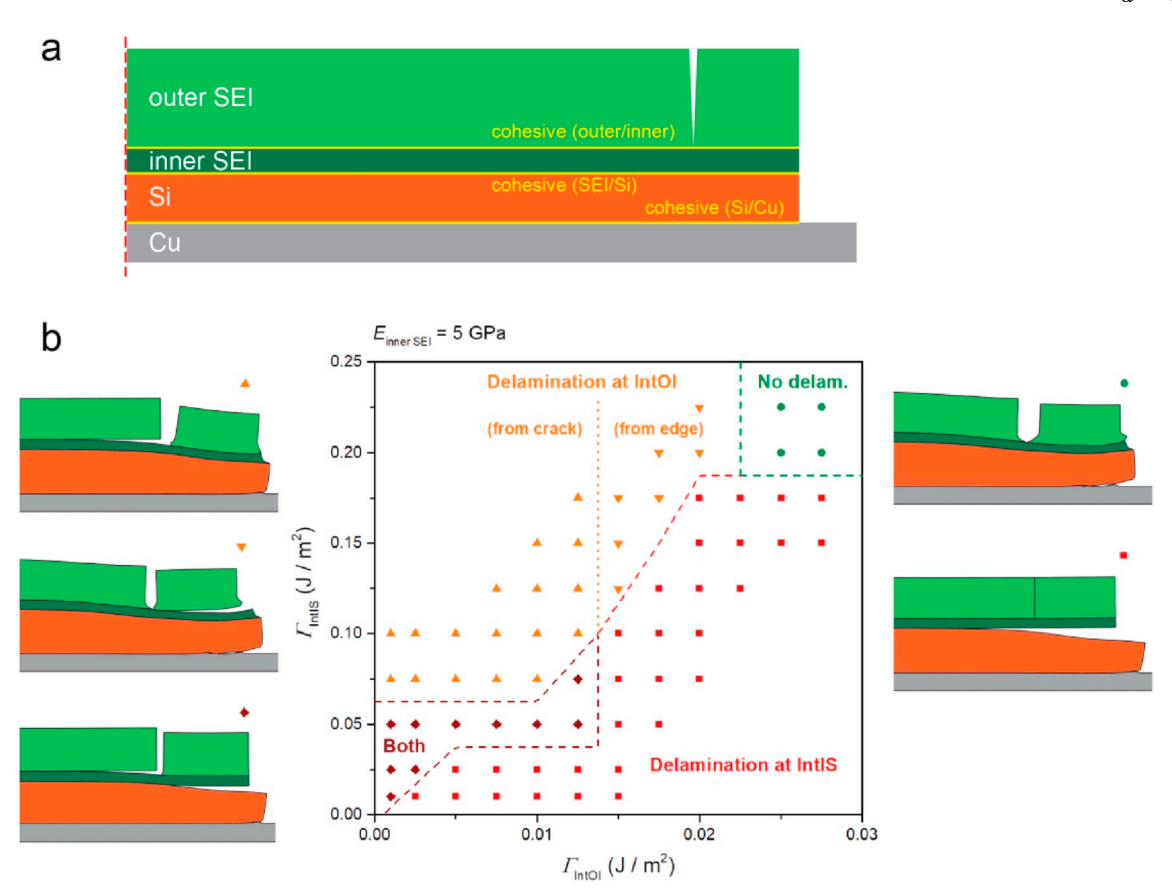


Fig. 7. (a) Schematic of the FEM. (b) Delamination map with Young's modulus of the inner SEI equal to 5 GPa (x- and y-axes correspond to the interfacial fracture toughness of IntOI and IntIS, respectively).

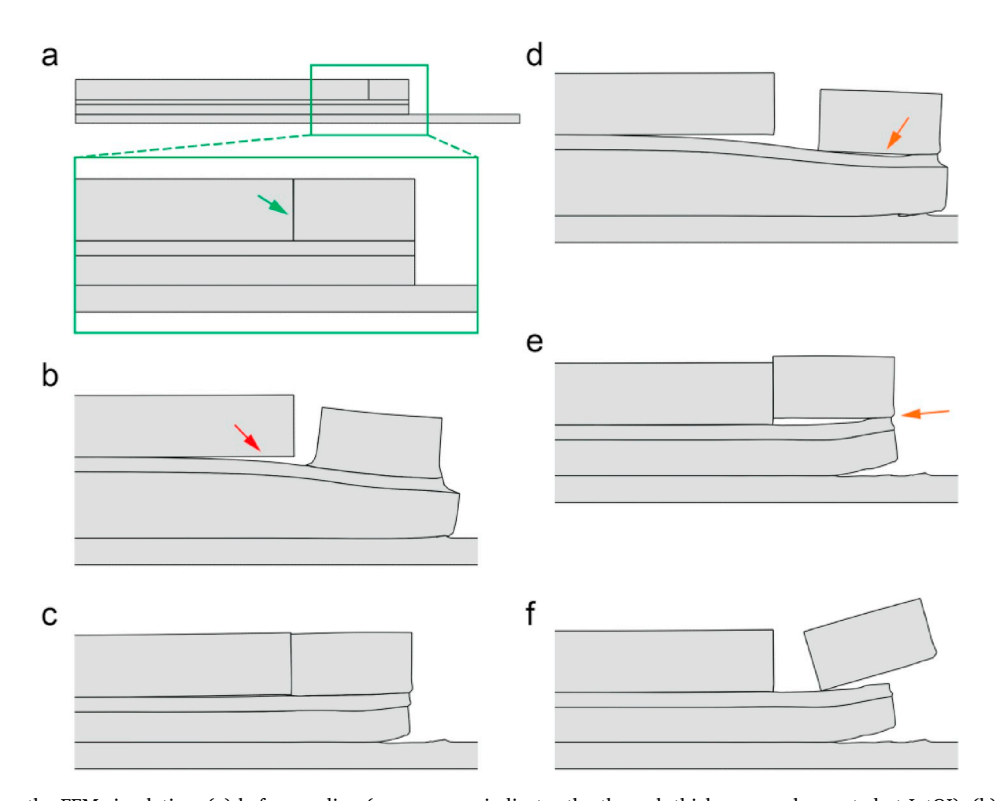


Fig. 8. Screenshots from the FEM simulation: (a) before cycling (green arrow indicates the through-thickness crack arrested at IntOI); (b) after the 1st lithiation cycle; (c) after the 1st delithiation cycle; (d) after the 2nd lithiation cycle; (e–f) during the 2nd delithiation cycle.

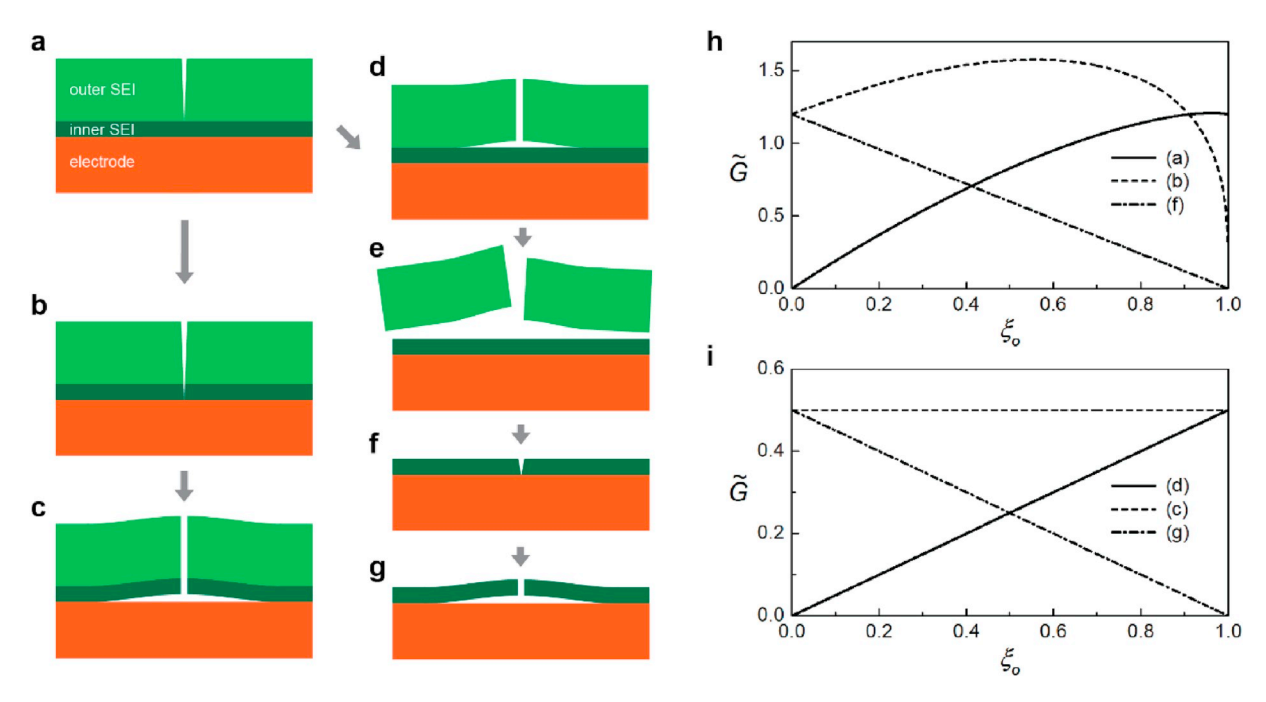


Fig. 9. Schematics of possible failure progression sequences in a bilayer SEI: (a) through-thickness cracking of the outer layer, (b) through-thickness cracking of the inner layer, (c) delamination between the inner layer and electrode, (d) delamination between the outer and inner layers, (e) spallation of the outer layer, (f) through-thickness cracking of the inner layer after spallation, (g) delamination between the inner layer and electrode after spallation. Normalized steady-state energy release rate for (h) crack channeling and (i) interfacial delamination as a function of the thickness fraction of the outer SEI layer.

steady-state is given by,

$$G^{b} = \frac{\sigma_{f}^{2} h_{f}}{\overline{E}_{f}} \frac{\int_{\xi_{o}}^{1} \tilde{g}(\tilde{a}_{f}) d\tilde{a}_{f}}{1 - \xi_{o}}.$$
 (5)

For $mode\,f$, the energy release rate of a steady-state channeling crack in the inner layer after the spallation of the outer layer can be calculated as,

$$G^{f} = \frac{\sigma_{f}^{2} h_{f}}{\overline{E}_{s}} (1 - \xi_{o}) \int_{0}^{1} \tilde{g}(\tilde{a}_{i}) d\tilde{a}_{i}, \tag{6}$$

where \tilde{a}_i is the plane strain crack length normalized by the thickness of the inner layer.

In terms of the interface modes c, d and g, unstable delamination occurs if the energy release rate of a steady-state interface crack G exceeds the interfacial toughness. For mode c,

$$G^c = \frac{1}{2} \frac{\sigma_f^2 h_f}{\overline{E}_f}.$$
 (7)

For mode d,

$$G^d = \frac{\xi_o}{2} \frac{\sigma_f^2 h_f}{\overline{E}_f}.$$
 (8)

For mode g

$$G^g = \frac{1 - \xi_o}{2} \frac{\sigma_f^2 h_f}{\overline{E}_f}.$$
 (9)

Equations (4)–(9) summarizes the steady-state energy release rates for $modes\ a$ -d, f and g. For a given value of ξ_o it can be observed that these energy release rates are all proportional to the SEI thickness as well as the square of the mismatch stress in the SEI and are inversely proportional to the SEI modulus.

All of the mechanisms scale with the strain energy density in the SEI layer, which leads to the following normalized energy release rate:

$$\tilde{G}(\xi_o) = \frac{G(\xi_o)}{\sigma_f^2 h_f / \overline{E}_f} \tag{10}$$

This form provides a convenient basis for comparing the different modes. The common scaling here indicates that thinner SEI is more resistant to all of these failure processes. Assessing the impact of the relative layer thicknesses requires evaluation of the different mechanisms. This can be considered by examining changes in the fraction of the outer layer ξ_0 while fixing all of the other properties including the total SEI thickness. Variations of the normalized energy release rate with ξ_0 are plotted in Fig. 9(h,i) for different failure modes. These results provide a basis for additional assessments of different mechanisms. Key examples of this are discussed further below. Comparison of \tilde{G} for mode a and b shows that cracking in the inner layer has a higher energy release rate than cracking in the outer layer unless the inner layer is much thinner ($\xi_0 > 90\%$). If we consider a stiffer inner layer with additional inorganic components formed, the energy release rate for *mode b* is even higher. However, fracture of the inner layer was not observed in the experiments reported here. This solidifies our hypothesis that the inner layer has a higher fracture toughness than the outer layer.

Fig. 9(h,i) shows that \tilde{G} for *mode b* and *mode c* are higher than those for *mode f* and *mode g*, respectively, indicating that spallation of the outer layer makes cracking and delamination of the inner layer less likely. The spallation of the outer layer was observed and analyzed in detail in previous sections. Based on the analysis in Fig. 9(h) and (i), it is likely that spallation of the outer layer promotes an inner SEI layer that remains intact and well adhered to the Si island.

The evaluation of the failure progressions in Fig. 9 inspires a new understanding of strategies that can be employed to build strain tolerant SEI layers. Based on the SEI formation process discussed previously [21], the outer SEI layer which forms first at higher voltages facilitates the formation of a tough and passivating nanocomposite inner layer. Once this structure is created the spallation of the outer layer is not necessarily problematic and can instead be advantageous both mechanically (by enhancing mechanical stability of the inner layer) and electrochemically

(by reducing impedance). Comparison of \check{G} for $mode\ b$ and $mode\ d$ shows that letting ξ_o approach 1 (i.e., making the inner layer as thin as possible) can suppress inner layer cracking and facilitate delamination and spallation of the outer layer. The minimum inner layer thickness will be largely dictated by its ability to passivate the surface against further SEI formation, which requires blocking electron conduction.

The preliminary analyses in this section demonstrate that the bilayer structure significantly affects the mechanical degradation mechanisms of the SEI layer. More accurate modeling requires further experimental information about mechanical properties of SEI layers (particularly plasticity) and consideration of intrinsic cracking mechanisms of SEI at the atomistic level. These are expected to be fruitful areas for future study.

5. Conclusions

In situ AFM, ex situ FIB measurements and finite element modeling were integrated to investigate the impact of lateral strains on SEI formation and degradation. A bilayer structure of the SEI on Si anodes was observed, and tensile stresses in the SEI layer resulted in throughthickness cracks that appear inside of the outer SEI and are arrested at the outer and inner SEI interface. The absence of cracking of the inner SEI layer implies its high fracture toughness. During cyclic lithiation and delithiation, interfacial delamination between the outer and inner SEI layers occurs while the inner layer is still well adhered to the underlying Si, which indicates that the interfacial toughness between the inner SEI and Si is much higher than that between the outer and inner SEI layers based on FEM calculations. The incremental delamination of the outer SEI layer with increasing cycle number, which is akin to plastic ratcheting, eventually leads to its spallation. The observation that the inner layer does not undergo substantial additional growth after spallation indicates that this thin inner layer can provide good passivation, even when large strains are applied during subsequent cycling. Detailed analysis of the bilayer system also reveals guidelines for producing an inner SEI layer that can simultaneously satisfy the electrochemical and mechanical criteria for stable passivation of silicon electrode surfaces. A more detailed understanding of the mechanical behavior of this inner SEI layer is expected to pave the way toward design of strain-tolerant SEIs.

Declaration of competing interest

None.

Acknowledgments

The authors acknowledge primary support from the Assistant Secretary for Energy Efficiency and Renewable Energy, Vehicle Technologies Office of the U.S. Department of Energy, Award Number DE-EE0007787 under the Battery Material Research (BMR) Program. Additional support was also provided by SK Innovation and the National Science Foundation (DMR-1832829).

Appendix A. Supplementary data

Supplementary data to this article can be found online at https://doi.org/10.1016/j.nanoen.2019.104257.

References

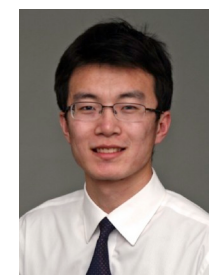
- [1] V. Etacheri, O. Haik, Y. Goffer, G.A. Roberts, I.C. Stefan, R. Fasching, D. Aurbach, Effect of fluoroethylene carbonate (FEC) on the performance and surface chemistry of Si-nanowire Li-ion battery anodes, Langmuir 28 (2012) 965–976.
- [2] Y.M. Lin, K.C. Klavetter, P.R. Abel, N.C. Davy, J.L. Snider, A. Heller, C.B. Mullins, High performance silicon nanoparticle anode in fluoroethylene carbonate-based electrolyte for Li-ion batteries, Chem. Commun. 48 (2012) 7268–7270.

[3] K. Schroder, J. Avarado, T.A. Yersak, J.C. Li, N. Dudney, L.J. Webb, Y.S. Meng, K. J. Stevenson, The effect of fluoroethylene carbonate as an additive on the solid electrolyte interphase on silicon lithium-ion electrodes, Chem. Mater. 27 (2015) 5531-5549

- [4] H. Wu, G.Y. Zheng, N.A. Liu, T.J. Carney, Y. Yang, Y. Cui, Engineering empty space between Si nanoparticles for lithium-ion battery anodes, Nano Lett. 12 (2012) 904–909
- [5] N. Liu, H. Wu, M.T. McDowell, Y. Yao, C.M. Wang, Y. Cui, A yolk-shell design for stabilized and scalable Li-ion battery alloy anodes, Nano Lett. 12 (2012) 3315–3321
- [6] J.Y. Luo, X. Zhao, J.S. Wu, H.D. Jang, H.H. Kung, J.X. Huang, Crumpled grapheneencapsulated Si nanoparticles for lithium ion battery anodes, J. Phys. Chem. Lett. 3 (2012) 1824–1829.
- [7] S. Menkin, D. Golodnitsky, E. Peled, Artificial solid-electrolyte interphase (SEI) for improved cycleability and safety of lithium-ion cells for EV applications, Electrochem. Commun. 11 (2009) 1789–1791.
- [8] X.C. Xiao, P. Lu, D. Ahn, Ultrathin multifunctional Oxide coatings for lithium ion batteries, Adv. Mater. 23 (2011) 3911–3915.
- [9] J.C. Li, N.J. Dudney, J. Nanda, C.D. Liang, Artificial solid electrolyte interphase to address the electrochemical degradation of silicon electrodes, ACS Appl. Mater. Interfaces 6 (2014) 10083–10088.
- [10] Y.M. Lee, J.Y. Lee, H.T. Shim, J.K. Lee, J.K. Park, SEI layer formation on amorphous si thin electrode during precycling, J. Electrochem. Soc. 154 (2007) A515–A519.
- [11] B. Philippe, R. Dedryvere, J. Allouche, F. Lindgren, M. Gorgoi, H. Rensmo, D. Gonbeau, K. Edstrom, Nanosilicon electrodes for lithium-ion batteries: interfacial mechanisms studied by hard and soft X-ray photoelectron spectroscopy, Chem. Mater. 24 (2012) 1107–1115.
- [12] M.Y. Nie, D.P. Abraham, Y.J. Chen, A. Bose, B.L. Lucht, Silicon solid electrolyte interphase (SEI) of lithium ion battery characterized by microscopy and spectroscopy, J. Phys. Chem. C 117 (2013) 13403–13412.
- [13] S. Chattopadhyay, A.L. Lipson, H.J. Karmel, J.D. Emery, T.T. Fister, P.A. Fenter, M. C. Hersam, M.J. Bedzyk, In situ X-ray study of the solid electrolyte interphase (SEI) formation on graphene as a model Li-ion battery anode, Chem. Mater. 24 (2012) 3038–3043.
- [14] S.S. Zhang, M.S. Ding, K. Xu, J. Allen, T.R. Jow, Understanding solid electrolyte interface film formation on graphite electrodes, Electrochem. Solid State Lett. 4 (2001) A206–A208.
- [15] S.S. Zhang, K. Xu, T.R. Jow, EIS study on the formation of solid electrolyte interface in Li-ion battery, Electrochim. Acta 51 (2006) 1636–1640.
- [16] P. Lu, C. Li, E.W. Schneider, S.J. Harris, Chemistry, impedance, and morphology evolution in solid electrolyte interphase films during formation in lithium ion batteries, J. Phys. Chem. C 118 (2014) 896–903.
- [17] J. Nanda, M.K. Datta, J.T. Remillard, A. O'Neill, P.N. Kumta, In situ Raman microscopy during discharge of a high capacity silicon-carbon composite Li-ion battery negative electrode, Electrochem. Commun. 11 (2009) 235–237.
- [18] Z.H. Zhu, Y.F. Zhou, P.F. Yan, R.S. Vemuri, W. Xu, R. Zhao, X.L. Wang, S. Thevuthasan, D.R. Baer, C.M. Wang, In situ mass spectrometric determination of molecular structural evolution at the solid electrolyte interphase in lithium-ion batteries, Nano Lett. 15 (2015) 6170–6176.
- [19] A. von Cresce, S.M. Russell, D.R. Baker, K.J. Gaskell, K. Xu, In situ and quantitative characterization of solid electrolyte interphases, Nano Lett. 14 (2014) 1405–1412.
- [20] A. Tokranov, B.W. Sheldon, C.Z. Li, S. Minne, X.C. Xiao, In situ atomic force microscopy study of initial solid electrolyte interphase formation on silicon electrodes for Li-ion batteries, ACS Appl. Mater. Interfaces 6 (2014) 6672–6686.
- [21] A. Tokranov, R. Kumar, C.Z. Li, S. Minne, X.C. Xiao, B.W. Sheldon, Control and optimization of the electrochemical and mechanical properties of the solid electrolyte interphase on silicon electrodes in lithium ion batteries, Adv. Energy Mater. 6 (2016), 1502302.
- [22] I. Yoon, D.P. Abraham, B.L. Lucht, A.F. Bower, P.R. Guduru, In situ measurement of solid electrolyte interphase evolution on silicon anodes using atomic force microscopy, Adv. Energy Mater. 6 (2016), 1600099.
- [23] Y.Z. Li, Y.B. Li, A.L. Pei, K. Yan, Y.M. Sun, C.L. Wu, L.M. Joubert, R. Chin, A.L. Koh, Y. Yu, J. Perrino, B. Butz, S. Chu, Y. Cui, Atomic structure of sensitive battery materials and Interfaces revealed by cryo-electron microscopy, Science 358 (2017) 506–510.
- [24] X.F. Wang, M.H. Zhang, J. Alvarado, S. Wang, M. Sina, B.Y. Lu, J. Bouwer, W. Xu, J. Xiao, J.G. Zhang, J. Liu, Y.S. Meng, New insights on the structure of electrochemically deposited lithium metal and its solid electrolyte interphases via cryogenic TEM, Nano Lett. 17 (2017) 7606–7612.
- [25] Y.Z. Li, W. Huang, Y.B. Li, A. Pei, D.T. Boyle, Y. Cui, Correlating structure and function of battery interphases at atomic resolution using cryoelectron microscopy, Joule 2 (2018) 2167–2177.
- [26] D. Aurbach, I. Weissman, A. Zaban, O. Chusid, Correlation between surfacechemistry, morphology, cycling efficiency and interfacial properties of Li electrodes in solutions containing different Li salts, Electrochim. Acta 39 (1994) 51–71.
- [27] D. Aurbach, A. Zaban, A. Schechter, Y. Eineli, E. Zinigrad, B. Markovsky, The study of electrolyte-solutions based on ethylene and diethyl carbonates for rechargeable Li batteries .1. Li metal anodes, J. Electrochem. Soc. 142 (1995) 2873–2882.
- [28] D. Aurbach, Review of selected electrode-solution interactions which determine the performance of Li and Li ion batteries, J. Power Sources 89 (2000) 206–218.
- [29] A.M. Andersson, K. Edstrom, Chemical composition and morphology of the elevated temperature SEI on graphite, J. Electrochem. Soc. 148 (2001) A1100–A1109.

- [30] P.B. Balbuena, Y. Wang, Lithium-ion Batteries: Solid-Electrolyte Interphase, Imperial College, London, 2004.
- [31] K. Edstrom, M. Herstedt, D.P. Abraham, A new look at the solid electrolyte interphase on graphite anodes in Li-ion batteries, J. Power Sources 153 (2006) 380–384
- [32] P. Lu, S.J. Harris, Lithium transport within the solid electrolyte interphase, Electrochem. Commun. 13 (2011) 1035–1037.
- [33] S.Q. Shi, P. Lu, Z.Y. Liu, Y. Qi, L.G. Hector, H. Li, S.J. Harris, Direct calculation of Li-ion transport in the solid electrolyte interphase, J. Am. Chem. Soc. 134 (2012) 15476–15487.
- [34] J. Zhang, R. Wang, X.C. Yang, W. Lu, X.D. Wu, X.P. Wang, H. Li, L.W. Chen, Direct observation of inhomogeneous solid electrolyte interphase on MnO anode with atomic force microscopy and spectroscopy, Nano Lett. 12 (2012) 2153–2157.
- [35] C. Pereira-Nabais, J. Swiatowska, A. Chagnes, F. Ozanam, A. Gohier, P. Tran-Van, C.S. Cojocaru, M. Cassir, P. Marcus, Interphase chemistry of Si electrodes used as anodes in Li-ion batteries, Appl. Surf. Sci. 266 (2013) 5–16.
- [36] K.W. Schroder, A.G. Dylla, S.J. Harris, L.J. Webb, K.J. Stevenson, Role of surface oxides in the formation of solid-electrolyte interphases at silicon electrodes for lithium-ion batteries, ACS Appl. Mater. Interfaces 6 (2014) 21510–21524.
- [37] Z. Liu, P. Lu, Q.L. Zhang, X.C. Xiao, Y. Qi, L.Q. Chen, A bottom-up formation mechanism of solid electrolyte interphase revealed by isotope-assisted time-offlight secondary ion mass spectrometry, J. Phys. Chem. Lett. 9 (2018) 5508–5514.
- [38] M. Boniface, L. Quazuguel, J. Danet, D. Guyomard, P. Moreau, P. Bayle-Guillemaud, Nanoscale chemical evolution of silicon negative electrodes characterized by low-loss STEM-EELS, Nano Lett. 16 (2016) 7381–7388.
- [39] E. Peled, D. Golodnitsky, G. Ardel, Advanced model for solid electrolyte interphase electrodes in liquid and polymer electrolytes, J. Electrochem. Soc. 144 (1997) 1208-1210
- [40] Y.L. He, H.J. Hu, K.F. Zhang, S. Li, J.H. Chen, Mechanical insights into the stability of heterogeneous solid electrolyte interphase on an electrode particle, J. Mater. Sci. 52 (2017) 2836–2848.
- [41] M. Tanaka, J.B. Hooper, D. Bedrov, Role of plasticity in mechanical failure of solid electrolyte interphases on nanostructured silicon electrode: insight from continuum level modeling, ACS Appl. Energy Mater. 1 (2018) 1858–1863.
- [42] R. Kumar, A. Tokranov, B.W. Sheldon, X.C. Xiao, Z.Q. Huang, C.Z. Li, T. Mueller, In situ and operando investigations of failure mechanisms of the solid electrolyte interphase on silicon electrodes, ACS Energy Lett. 1 (2016) 689–697.
- [43] R. Kumar, P. Lu, X.C. Xiao, Z.Q. Huang, B.W. Sheldon, Strain-induced lithium losses in the solid electrolyte interphase on silicon electrodes, ACS Appl. Mater. Interfaces 9 (2017) 28406–28417.
- [44] X. Xiao, P. Liu, M.W. Verbrugge, H. Haftbaradaran, H. Gao, Improved cycling stability of silicon thin film electrodes through patterning for high energy density lithium batteries, J. Power Sources 196 (2011) 1409–1416.
- [45] S.K. Soni, B.W. Sheldon, X.C. Xiao, M.W. Verbrugge, D. Ahn, H. Haftbaradaran, H. J. Gao, Stress mitigation during the lithiation of patterned amorphous Si islands, J. Electrochem. Soc. 159 (2012) A38–A43.
- [46] K.J. Zhao, M. Pharr, J.J. Vlassak, Z.G. Suo, Inelastic hosts as electrodes for high-capacity lithium-ion batteries, J. Appl. Phys. 109 (2011), 016110.
- [47] H. Haftbaradaran, X.C. Xiao, M.W. Verbrugge, H.J. Gao, Method to deduce the critical size for interfacial delamination of patterned electrode structures and application to lithiation of thin-film silicon islands, J. Power Sources 206 (2012) 357–366.
- [48] H. Haftbaradaran, X.C. Xiao, H.J. Gao, Critical film thickness for fracture in thinfilm electrodes on substrates in the presence of interfacial sliding, Model. Simul. Mater. Sci. Eng. 21 (2013), 074008.
- [49] F. Fan, S. Huang, H. Yang, M. Raju, D. Datta, V.B. Shenoy, A.C.T. van Duin, S. Zhang, T. Zhu, Mechanical properties of amorphous LixSi alloys: a reactive force field study, Model. Simul. Mater. Sci. Eng. 21 (2013), 074002.
- [50] E. Rejovitzky, C.V. Di Leo, L. Anand, A theory and a simulation capability for the growth of a solid electrolyte interphase layer at an anode particle in a Li-ion battery, J. Mech. Phys. Solids 78 (2015) 210–230.
- [51] Z. Jia, T. Li, Failure mechanics of a wrinkling thin film anode on a substrate under cyclic charging and discharging, Extrem. Mech. Lett. 8 (2016) 273–282.
- [52] J.C. Wen, Y.J. Wei, Y.T. Cheng, Stress evolution in elastic-plastic electrodes during electrochemical processes: a numerical method and its applications, J. Mech. Phys. Solids 116 (2018) 403–415.
- [53] L. Yang, H. Chen, H. Jiang, Y. Wei, W. Song, D. Fang, Failure mechanisms of 2D silicon film anodes: in situ observations and simulations on crack evolution, Chem. Commun. 54 (2018) 3997–4000.
- [54] K. Guo, W. Zhang, B.W. Sheldon, H. Gao, Concentration dependent properties lead to plastic ratcheting in thin island electrodes on substrate under cyclic charging and discharging, Acta Mater. 164 (2019) 261–271.
- [55] P.H.L. Notten, F. Roozeboom, R.A.H. Niessen, L. Baggetto, 3-D integrated all-solidstate rechargeable batteries, Adv. Mater. 19 (2007) 4564–4567.
- [56] L. Baggetto, J.F.M. Oudenhoven, T. van Dongen, J.H. Klootwijk, M. Mulder, R.A. H. Niessen, M.H.J.M. de Croon, P.H.L. Notten, On the electrochemistry of an anode stack for all-solid-state 3D-integrated batteries, J. Power Sources 189 (2009) 402–410.
- [57] F. Luo, G. Chu, X.X. Xia, B.N. Liu, J.Y. Zheng, J.J. Li, H. Li, C.Z. Gu, L.Q. Chen, Thick solid electrolyte interphases grown on silicon nanocone anodes during slow cycling and their negative effects on the performance of Li-ion batteries, Nanoscale 7 (2015) 7651–7658.
- [58] H. Shin, J. Park, S. Han, A.M. Sastry, W. Lu, Component-/structure-dependent elasticity of solid electrolyte interphase layer in Li-ion batteries: experimental and computational studies, J. Power Sources 277 (2015) 169–179.

- [59] D. Bedrov, O. Borodin, J.B. Hooper, Li+ transport and mechanical properties of model solid electrolyte interphases (SEI): insight from atomistic molecular dynamics simulations, J. Phys. Chem. C 121 (2017) 16098–16109.
- [60] I. Yoon, S. Jurng, D.P. Abraham, B.L. Lucht, P.R. Guduru, Measurement of mechanical and fracture properties of solid electrolyte interaphase on lithium metal anodes in lithium ion batteries, Energy Storage Mater. (2019) in Press.
- [61] M.S. Hu, A.G. Evans, The cracking and decohesion of thin-films on ductile substrates, Acta Metall. Mater. 37 (1989) 917–925.
- [62] J.W. Hutchinson, Z. Suo, Mixed-mode cracking in layered materials, Adv. Appl. Mech. 29 (1992) 63–191.
- [63] J.L. Beuth, Cracking of thin bonded films in residual tension, Int. J. Solids Struct. 29 (1992) 1657–1675.
- [64] T. Nakamura, S.M. Kamath, 3-Dimensional effects in thin-film fracture-mechanics, Mech. Mater. 13 (1992) 67–77.
- [65] T. Ye, Z. Suo, A.G. Evans, Thin film cracking and the roles of substrate and interface, Int. J. Solids Struct. 29 (1992) 2639–2648.
- [66] J.L. Beuth, N.W. Klingbeil, Cracking of thin films bonded to elastic-plastic substrates, J. Mech. Phys. Solids 44 (1996) 1411–1428.
- [67] M. Huang, Z. Suo, Q. Ma, Plastic ratcheting induced cracks in thin film structures, J. Mech. Phys. Solids 50 (2002) 1079–1098.
- [68] J.J. Vlassak, Channel cracking in thin films on substrates of finite thickness, Int. J. Fract. 119 (2003) 299–323.
- [69] V.B. Shenoy, P. Johari, Y. Qi, Elastic softening of amorphous and crystalline Li-Si Phases with increasing Li concentration: a first-principles study, J. Power Sources 195 (2010) 6825–6830.
- [70] V.A. Sethuraman, M.J. Chon, M. Shimshak, V. Srinivasan, P.R. Guduru, In situ measurements of stress evolution in silicon thin films during electrochemical lithiation and delithiation, J. Power Sources 195 (2010) 5062–5066.
- [71] J. Dolbow, M. Gosz, Effect of out-of-plane properties of a polyimide film on the stress fields in microelectronic structures, Mech. Mater. 23 (1996) 311–321.
- [72] D.Y.W. Yu, F. Spaepen, The yield strength of thin copper films on Kapton, J. Appl. Phys. 95 (2004) 2991–2997.



Kai Guo received his B.Eng. degree from the Tsinghua University in 2012, and his Ph.D. degree in Engineering Science from the Brown University in 2019. At present, he is a post-doctoral researcher at MIT. His research interest is focused on mechanical degradation mechanisms in energy storage materials, and multiscale design of biomaterials and composites using machine learning.



Ravi Kumar received his B. Tech. degree in Materials Science and Engineering from IIT Kanpur, India in 2008 and then worked at Tata R&D in India for 3 years. He received his M.S. and Ph.D. degrees in Materials Engineering from Brown University in 2014 and 2018, respectively. At present, he is a process engineer in ALD Oxide group at Lam Research, Oregon.



Xingcheng Xiao is a staff researcher at General Motors Global R&D center with expertise on energy storage materials and surface engineering. He has published over 150 peer reviewed journal papers. He has over 60 granted patents and 40 pending patent applications in different fields. He is the recipient of Alexander von Humboldt Fellowship, R&D 100 Awards (2015 and 2017), and SME Innovations That Could Change the Way We Manufacture (2011).



Brian W. Sheldon is Professor of Engineering at Brown University. He received his S.B. (Chemical Engineering) and Sc.D. (Materials Science) from M.I.T. Before joining Brown, he was a research staff member at Oak Ridge National Laboratory. His recent research on the chemo-mechanics of energy storage materials is supported by the U.S. Department of Energy, the National Science Foundation, General Motors, Samsung, and SK Innovation



Huajian Gao received his B.S. degree from the Xi'an Jiaotong University of China in 1982, and his M.S. and Ph.D. degrees in Engineering Science from the Harvard University in 1984 and 1988, respectively. At present, he is Distinguished University Professor of Nanyang Technological University and Scientific Director of the Institute of High Performance Computing in Singapore. His research is focused on the understanding of basic principles that control mechanical properties and behaviors of materials in both engineering and biological systems.